

INTERNATIONAL SUMMER SCHOOL ON
INTELLIGENT SIGNAL PROCESSING FOR FRONTIER RESEARCH AND INDUSTRY
HUAZHONG UNIVERSITY OF SCIENCE AND TECHNOLOGY, HUST, AT WUHAN, CHINA
12–26 MAY 2019

Design and fabrication of Low Gain Avalanche Detectors (LGAD): a TCAD simulation study

K. Wu,^{a,b,1} M. Zhao,^{a,c} T. Yang,^{a,b} João Guimarães da Costa,^a Z. Liang^{a,c} and X. Shi^{a,c}
on behalf of IHEP HGTD collaboration

^a*Institute of High Energy Physics (IHEP), Chinese Academy of Sciences,
Beijing 100049, People's Republic of China*

^b*University of Chinese Academy of Sciences (UCAS),
Beijing 100049, People's Republic of China*

^c*State Key Laboratory of Particle Detection and Electronics,
Beijing 100049, People's Republic of China*

E-mail: wukw@ihep.ac.cn

ABSTRACT: Low Gain Avalanche Detectors (LGAD) are silicon sensors with a time resolution better than 20 ps. The ATLAS and CMS experiments are designing LGAD detectors to address the pile-up challenge at the High Luminosity-Large Hadron Collider (HL-LHC). The Institute of High Energy Physics (IHEP) High-Granularity Timing Detector group has recently developed its first version of LGAD sensors. The LGAD structure was designed using Technology Computer-Aided Design (TCAD) simulations and optimized to obtain a high breakdown voltage and ideal gain. The n-type Junction Termination Extension (N-JTE) zone is a critical structure to guarantee a high breakdown voltage. The gain layer is optimized for an ideal gain factor and hence good time resolution. The optimized LGAD sensor has a gain higher than six and a breakdown voltage higher than 400 V.

KEYWORDS: Solid state detectors; Timing detectors; Charge transport and multiplication in solid media; Photon detectors for UV, visible and IR photons (solid-state) (PIN diodes, APDs, Si-PMTs, G-APDs, CCDs, EBCCDs, EMCCDs, CMOS imagers, etc)

¹Corresponding author.

Contents

1	Introduction	1
2	Structure	1
3	TCAD simulation of the electrical characteristics	2
3.1	Structure optimization	3
3.1.1	JTE size	3
3.1.2	JTE to P-stop distance	5
3.1.3	Field plate	5
3.1.4	Layout mask	7
3.2	Doping profile optimization	7
3.2.1	Gain layer diffusion process optimization	8
3.2.2	Gain layer implantation process optimization	8
4	Fabrication process	9
5	Summary	11

1 Introduction

The High Luminosity (HL) Phase-II of the Large Hadron Collider (LHC) at CERN is scheduled to start in 2026. This HL-LHC will deliver an integrated luminosity of up to 4000 fb^{-1} over the subsequent decade. The instantaneous luminosity of the HL-LHC will reach up to $7.5 \times 10^{34} \text{ cm}^{-2}\text{s}^{-1}$, a substantial increase from the $2.1 \times 10^{34} \text{ cm}^{-2}\text{s}^{-1}$ obtained during LHC Run 2 [1, 2]. This will cause a significant increase in the pile-up, calling for improved spatial and timing resolution of the sensors in order for particle tracks to be distinguished and primary vertices to be properly identified. One possible approach to cope with these requirements is using tracking sensors with high timing capabilities. The LGAD sensors are silicon sensors with a time resolution better than 20 ps. They have so far been developed by several silicon foundries [3–8]. The Institute of High Energy Physics (IHEP) High-Granularity Timing Detector group has recently developed its first version of LGAD sensors. In this paper, we report on the design, Technology Computer-Aided Design (TCAD) simulation and proposed fabrication technology for these devices.

2 Structure

The LGAD structure drawn in figure 1 is based on the standard PIN diode architecture with an n^{++} layer as the cathode and a p^{++} layer as the anode. High voltage is applied on the anode and charge is collected from the n^{++} cathode at the ground.

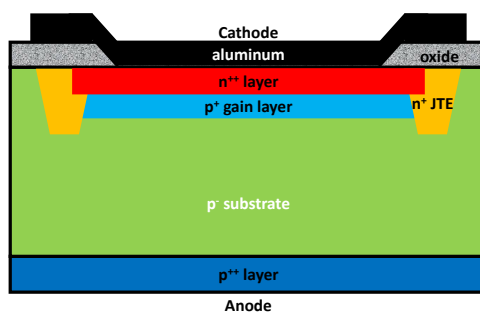


Figure 1. Sketch of the structure of an LGAD (not to scale) with the active area shown.

The p^- substrate is the active volume for charge drifting. Its thickness contributes to the sensor's time resolution [1] because a thin sensor will have a shorter charge drift time. Directly under the n^{++} layer, a special gain layer composed of a p-type dopant delivers a low gain factor (10 ~ 20). Besides the sensor's thickness, the proper gain factor is another key contributor in controlling the time resolution [1]. At the edge of the n^{++} and p^+ regions a high electric-field forms due to the beveled edge terminations. The Junction Termination Extension (JTE) [9] made by an n^+ dopant can alter the surface electric field at the edges by selectively adding the charge to the junction. The p-stop [10] diffusion plotted in figure 2 can eliminate the electrical connection among n-type diffusions due to the surface inversion layer. Guard rings are added at the device's periphery to shape the electric field distribution at the junction edges and shield the active area from the lateral leakage current [11].

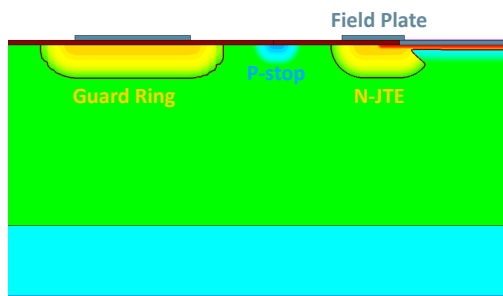


Figure 2. Cross section of an LGAD at the periphery showing doping concentrations of different regions.

3 TCAD simulation of the electrical characteristics

Our design study is based on TCAD. TCAD is a group of software tools aimed at process and device analysis and optimization. In case of LGADs, TCAD has been already successfully used by different groups, see e.g. [12, 13]. In our study, Sentaurus Structure Editor (SDE) was used to draw sensor models with the ideal geometry. In the Sentaurus Structure Editor, we choose the “select region” as a boundary condition, which means all boundary edges or boundary faces will be assigned to the contact. Sentaurus Process (sprocess) is used to draw sensor structures from process fabrication. Sentaurus Device (sdevice) is used to perform electrical characterization simulations.

There are different physics models for users to choose from. For example, in sdevice's Physics Mobility section we used a physics model "DopingDep" which causes the mobility degradation due to impurity scattering. In sdevice Physics Recombination SRH section, we used a physics model "TempDep" which activates the temperature behavior depending on the nature of the recombination centers. Sentaurus Visual (svisual) is a visualization tool used to analyze the sensor doping profile, breakdown voltage, current density, electrical field and others.

The electrical characterization simulation (with sdevice) includes current-voltage (IV) simulation and gain simulation. Both simulations are performed by applying a negative high voltage on the anode and collecting the signals from the cathode. The IV simulation (in figure 3) calculates the current going through the sensor at different voltages and provides the depletion voltage, leakage current, breakdown voltage, electric field distribution, current density and others. The gain simulation is based on a Minimal Ionizing Particle (MIP) signal (shown in figure 4). The gain is equal to the total collected charge divided by the MIP's primary ionizing charge (3.1). The MIP signal was set with the "HeavyIon" model and injected vertically into the center of the cathode.

$$\text{Gain} = \frac{Q_{\text{total}}}{Q_{\text{primary}}} \quad (3.1)$$

In the electrical characterization simulation, the design is optimized by first adjusting the sensor structure, and then doping profile and then checking its electrical performance.

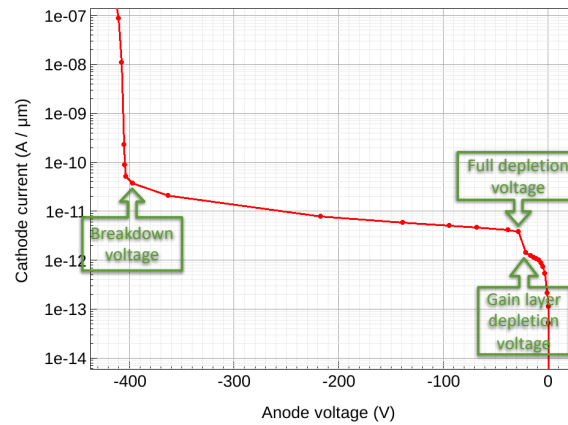


Figure 3. In this IV simulation, the cathode's current is plotted against the bias voltage. The gain layer is fully depleted at -21 V. The sensor is fully depleted at -28 V, and the breakdown occurs at -395 V.

3.1 Structure optimization

Structure optimization was mainly done with SDE and sdevice tools. The sensor structures generated with SDE are analyzed with sdevice. Sdevice is used to electrically analyze the sensor and svisual for visualization analysis.

3.1.1 JTE size

The Junction Termination Extension (JTE) is a critical structure to shape the electric field at the electrode's edge and to protect the sensor from an early breakdown. A round, deep and wide JTE

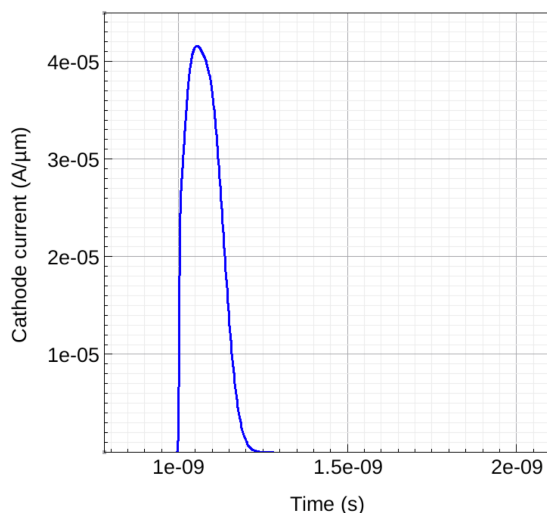


Figure 4. The transient simulation of the MIP signal at 1 ns is plotted above as the cathode current over time. The gain factor can be extracted through an integration of current after removing the leakage current offset.

structure can help the sensor have a high breakdown voltage. In the real fabrication process, some process conditions will limit the JTE shape. The region from JTE to the edge of the sensor is a dead area not sensitive to high energy particles. In the ATLAS High-Granularity Timing Detector (HGTD) the LGAD sensor pad size is $1.3 \text{ mm} \times 1.3 \text{ mm}$. The larger the JTE, the lower the fill factor, hence the lower the detection efficiency. As an example, figure 5 shows the fill factor as a function of the JTE width for a fixed distance between JTE and sensor edge of $80 \mu\text{m}$.

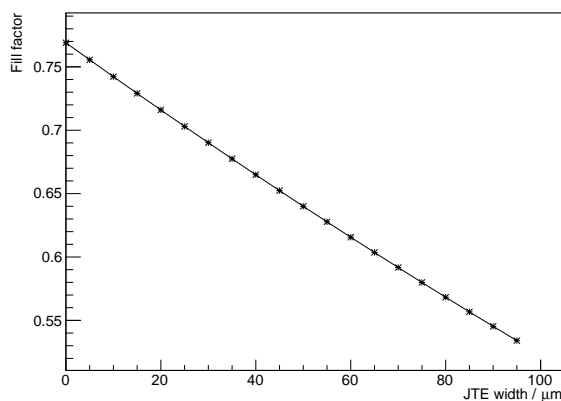


Figure 5. The fill factor is plotted above against different JTE widths. The pad size is $1.3 \text{ mm} \times 1.3 \text{ mm}$ and the distance from the JTE to the sensor edge is $80 \mu\text{m}$.

IHEP is collaborating with the Tianjin Zhonghuan Semiconductor Company [14] to fabricate this LGAD sensor. IHEP has optimized the JTE process to obtain a high breakdown voltage using the Zhonghuan process. In this process, ion implantation is limited to low energies. Even with an extended thermal diffusion process, the depths of each junction are limited to several microns.

The JTE width is one of the few parameters that control breakdown voltage in this sensor. IV simulations were done to optimize the JTE width as shown in figure 6.

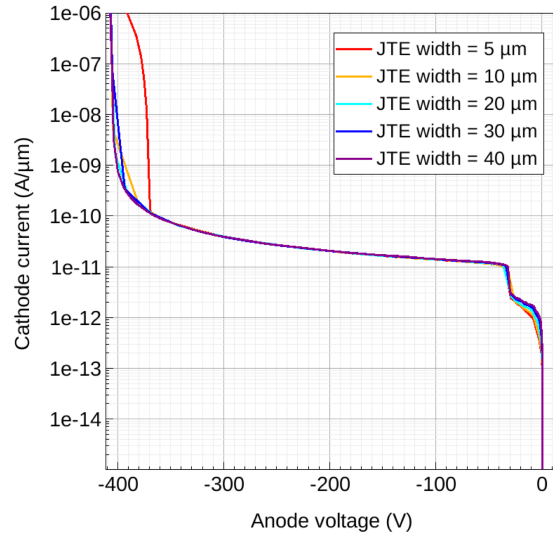


Figure 6. The sensor with JTE width of 5 micron breaks down before -400 V. The JET width should be equal or larger than 10 micron.

The sensor begins breaking down at a lower voltage when the JTE width is less than $10\ \mu\text{m}$. Taking into consideration both early breakdown issues caused by a narrow JTE and low fill factor issues caused by a wide JTE, only a JTE with a width of $20\ \mu\text{m}$, $30\ \mu\text{m}$, $50\ \mu\text{m}$, and $80\ \mu\text{m}$ were used in the final design. Simulations were done in a 2D structure. For TCAD electrical simulation, the 2D sensor model has a higher breakdown voltage than a 3D sensor model having the same doping profile and size. The JTE ring in the 3D sensor model and the real sensor has four corners called spherical junctions [15]. Those spherical junctions will have a higher electrical field than the cylinder region in 2D simulations which cause early breakdown. Wider JTE structures were used to eliminate this effect caused by the difference between 2D and 3D models.

3.1.2 JTE to P-stop distance

Similar to the JTE width, the distance between the p-stop and the JTE affects the sensor performance. Longer distances mean less fill factor. Less distances lead to early breakdowns as figure 7 shows; $30\ \mu\text{m}$ is the minimum distance to prevent early breakdown.

3.1.3 Field plate

With the application of the field plate, it is possible to approach the breakdown voltage of a parallel-plane junction. The field plate structure is shown in figure 2 which extends the contact metal for the n^{++} electrode over the field oxide at the edge. This plate produces an expansion of the depletion region along the surface. The resulting reduction in the electric field at the JTE increases the breakdown voltage. The junction depth corresponding to an oxide thickness of t_{ox} is given by (3.2) [15].

$$x_J = \left(\frac{\epsilon_{\text{Si}}}{\epsilon_{\text{ox}}} \right) t_{\text{ox}} \approx 3t_{\text{ox}} \quad (3.2)$$

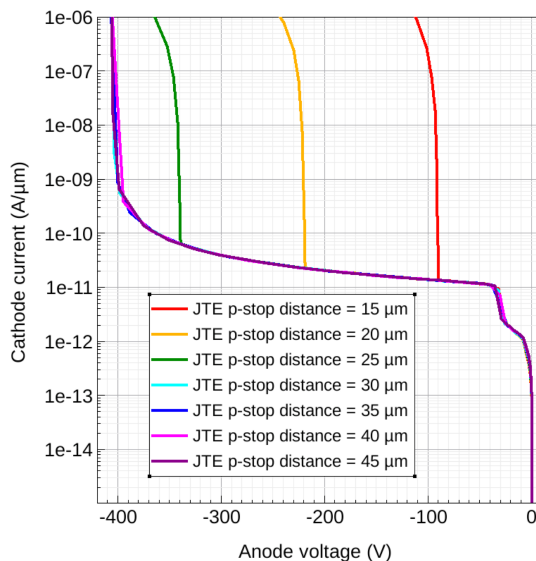


Figure 7. The IV simulation with different JTE to P-stop distances. A sensor with a distance shorter than $30\ \mu\text{m}$ breaks down earlier than $-400\ \text{V}$. In these simulations, the JTE width is $10\ \mu\text{m}$, and the p-stop width is $2\ \mu\text{m}$.

The field oxide thickness is one-third of the junction depth. For example, the breakdown voltage at the field plate for a field oxide thickness of $1\ \mu\text{m}$ would be equivalent to the breakdown voltage of a cylindrical junction with a depth of $3\ \mu\text{m}$. Our sensor oxide layer thickness is $0.94\ \mu\text{m}$. The oxide charge used in simulation is 0. This choice is appropriate for the pre-irradiation conditions, since the typical oxide charge density that the foundry can ensure is lower than $10^{10}\ \text{cm}^{-2}$. The field plate size, and especially its edge, also determines the breakdown voltage. IV simulation for different field plate sizes (figure 8) reveals the highest breakdown voltage is achieved with a field plate edge located $517\ \mu\text{m}$ from the sensor center.

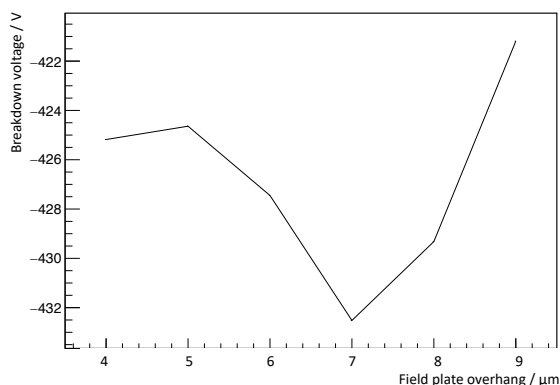


Figure 8. The field plate edge optimization is shown above by plotting the field plate overhang against the breakdown voltage. The field plate overhang is the distance between the JTE mask outside edge and the field plate edge. The highest breakdown voltage is achieved with a field plate overhang of $7\ \mu\text{m}$. In these simulations, the JTE width is $10\ \mu\text{m}$, the p-stop width is $2\ \mu\text{m}$, and the JTE p-stop distance is $29\ \mu\text{m}$.

3.1.4 Layout mask

Different structure designs were included in the layout mask shown in figure 9. Table 1 shows the details of different designs. IV measurements, capacitance-voltage measurements, and gain measurements reveal the best structure design for this LGAD sensor.

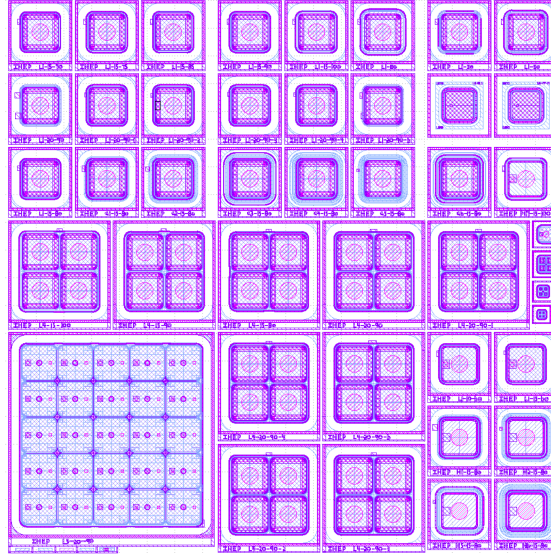


Figure 9. The layout mask for fabricating the LGAD sensor is shown above. The mask includes single pads, 2×2 , and 5×5 arrays.

Table 1. Different designs in layout mask.

Pixel number	JTE width (μm)	JTE and Pstop distance (μm)	Field plate and guard rings
Single	15	18, 20.5, 23, 25.5, 28, 33	without FP, same guard ring
Single	20	23	5 types FP, same guard ring
Single	15, 20, 30, 50, 80	33	without FP, same guard ring
Single	15	25	5 guard ring
2×2	15	23, 28, 33	without FP, same guard ring
2×2	20	23	5 types FP, same guard ring
5×5	20	23	without FP

3.2 Doping profile optimization

In the doping profile optimization, different from structure optimization, sprocess was used to obtain sensor models close to the real sensors fabricated by the foundry. Sdevice was used to electrically analyze the sensor and svisual for the visualization analysis. Structure optimization was done in the dead area including JTE, P-stop, field plate and guard ring. Those structure optimizations can reduce the risk of early breakdown occurring in dead areas. The doping profile is optimized in the active area including the n^{++} and p^+ layer. Figure 10 shows the n^{++} layer and p^+ layer doping concentration distribution at different depths. The n^{++} layer works as a charge collection electrode

which only needs to be highly doped in the shallow region. Most doping optimization studies were done in the p^+ gain layer to obtain special gain.

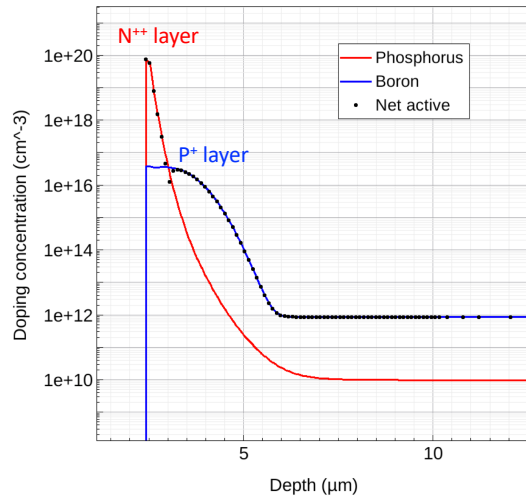


Figure 10. N^{++} layer and p^+ layer doping concentration distribution in different depths. Phosphorus is used as the n-type dopant. Boron is used as the p-type dopant.

3.2.1 Gain layer diffusion process optimization

For making the p^+ layer as a gain layer, the p-type doping concentration needs to be higher than $1 \times 10^{16} \text{ cm}^{-3}$. Going to the deeper region to avoid overlapping with the n^{++} layer can increase active p-type doping concentration. However, in the foundry process condition, the ion implantation energy is not high enough to inject p-type dopants into an adequately deep region. Without high energy injection, a deep and precise highly doped p^+ layer could be achieved by long-time high-temperature diffusion. Figure 11 shows the p^+ gain layer depth increase as the diffusion time grows. Longer diffusion could diffuse dopant to deeper regions but also can lose maximum value which is higher than $1 \times 10^{16} \text{ cm}^{-3}$. According to the Zhonghuan process condition, the maximum diffusion temperature is 1150 Celsius. The gain layer implantation was done with $4.8 \times 10^{12} \text{ cm}^{-2}$ of boron. With 1150 Celsius diffusion, the sensor begins to obtain a higher multiplication coefficient in the same working voltage. After 2 hours of diffusion, the sensor starts to break down before -400 V as figure 12 shows. Breakdown happens in the active volume which can be simplified as a PN diode. The relation between the multiplication coefficient and the breakdown voltage is shown in (3.3) [15]. The active p-type dopant grows with diffusion time. The bias voltages need for getting the same multiplication coefficient become lower with the active p-type dopant grows. The breakdown voltages will become lower after long time diffusion.

$$M = \frac{1}{1 - (V/BV)^4} \quad (3.3)$$

3.2.2 Gain layer implantation process optimization

The ion implantation process has two main condition parameters: injection energy and injection dose. As maximum injection energy is limited, the injection dose dominates the sensor electrical

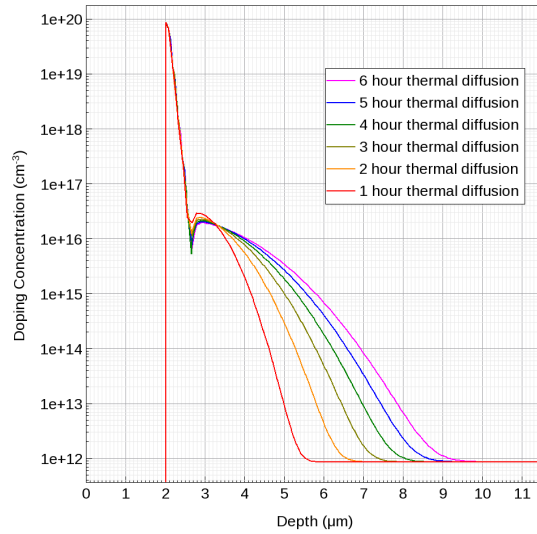


Figure 11. Doping concentration versus different depths from one to six hour 1150 celsius thermal diffusion. Gain layer boron doping concentration higher than $1 \times 10^{16} \text{ cm}^{-3}$.

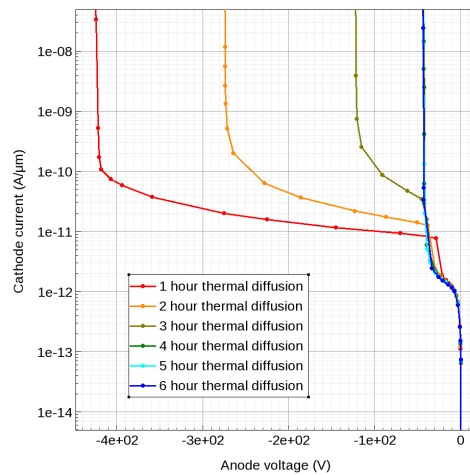


Figure 12. IV simulation with different thermal diffusion time. Sensors with diffusion time longer than one hour start to break down before -400 V .

characterization mainly on gain factor and breakdown voltage. A highly doped gain layer will increase the gain factor but also will suffer early breakdown issues which in turn shrinks the working voltage region and therefore decrease the gain. Figure 13 shows the sensor's gain at 300 V, 350 V and 400 V with different injection doses. The result indicates a reasonable gain above 6 can be obtained from the dose range ($4.8\text{--}5.2 \times 10^{12} \text{ cm}^{-2}$) for the ion implantation fabrication process.

4 Fabrication process

The final design will be produced by six different masks as figure 9 shows in overlapped mode. The first mask is the N-JTE and guard ring mask for n-type structure. The second mask is the p-stop

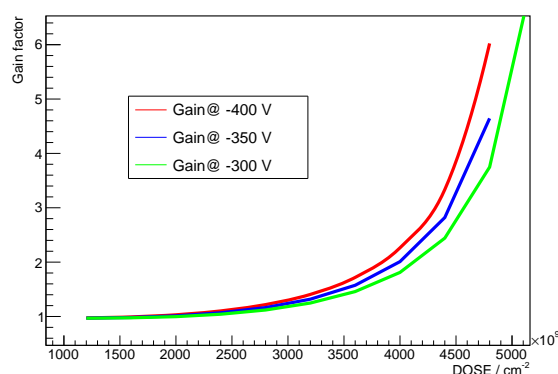


Figure 13. Gain factor versus different ion implantation doses for three anode voltages. A gain factor above six has been achieved with a dose range of $4.8\text{--}5.2 \times 10^{12} \text{ cm}^{-2}$.

mask for producing p-stop. The third one is the p^+ layer mask for the gain layer. The fourth one is the n^{++} layer mask for the n^{++} charge collection electrode. The fifth one is the etching oxide mask for exposing the electrode under the oxide layer. The last one is the metal contact mask for electrical connection. The metal mask is important especially for 5×5 sensor bump bonding with ASIC and for connecting with the probe card.

The fabrication process includes the following steps:

1. Deposit photoresist
2. Lithography with N-JTE and guard ring mask
3. Implant phosphorus
4. Thermal diffuse N-JTE and guard ring
5. Etch all photoresist
6. Deposit photoresist
7. Lithography with the p-stop mask
8. Implant boron
9. Etch all photoresist
10. Thermal grow oxide in wet oxygen (long time)
11. Deposit photoresist
12. Lithography with p^+ layer mask
13. Implant boron
14. Thermal diffuse p^+ layer

15. Etch all photoresist
16. Deposit photoresist
17. Lithography with n^{++} layer mask
18. Implant phosphorus
19. Thermal diffuse n^{++} layer (short time)
20. Etch all photoresist
21. Deposit photoresist
22. Lithography with etching oxide mask
23. Etch oxide
24. Etch all photoresist
25. Deposit aluminum with the metal mask

5 Summary

This paper presents a new effort by IHEP, in collaboration with Zhonghuan Company, to design suitable LGAD sensors. The LGAD design was constrained to satisfy the requirement of the ATLAS HGTD. The ATLAS HGTD requires new LGAD sensors with high-radiation resistance and a large fill factor. The sensor pad size is $1.3 \text{ mm} \times 1.3 \text{ mm}$. After TCAD simulation, LGAD sensors designed with gain higher than six and breakdown voltage higher than 400 V are being fabricated. Time resolution and radiation performance measurements will soon follow.

Acknowledgments

The authors would like to acknowledge: the funding by the State Key Laboratory of Particle Detection and Electronics, SKLPDE-ZZ-201911 project and SKLPDE-ZZ-202001 project; the colleagues from the HGTD IHEP group for their guidance and support; the department of Microelectronics and Nanoelectronics, Tsinghua University for their advice and resources [14]; Wanli Wang and Zixu Dong from Tianjin Zhonghuan Semiconductor Co., Ltd. for their help on device fabrication; the INFIERI committee for supporting the first author to participate in the 5th Summer School on Intelligent signal processing for FrontIER Research and Industry.

References

- [1] ATLAS collaboration, *Technical Proposal: A High-Granularity Timing Detector for the ATLAS Phase-II Upgrade*, [CERN-LHCC-2018-023](#), LHCC-P-012, CERN, Geneva (2018).
- [2] CMS collaboration, *Technical Proposal for a MIP timing detector in the CMS experiment phase 2 upgrade*, [CERN-LHCC-2017-027](#), LHCC-P-009, CERN, Geneva (2017).

- [3] G. Pellegrini et al., *Technology developments and first measurements of Low Gain Avalanche Detectors (LGAD) for high energy physics applications*, *Nucl. Instrum. Meth. A* **765** (2014) 12.
- [4] H.F.W. Sadrozinski et al., *Ultra-fast silicon detectors*, *Nucl. Instrum. Meth. A* **730** (2013) 226.
- [5] G. Giacomini, W. Chen, F. Lanni and A. Tricoli, *Development of a technology for the fabrication of Low-Gain Avalanche Diodes at BNL*, *Nucl. Instrum. Meth. A* **934** (2019) 52 [[arXiv:1811.04152](#)].
- [6] S. Wada, K. Ohnaru, K. Hara, J. Suzuki, Y. Unno, K. Nakamura et al., *Evaluation of characteristics of hamamatsu low-gain avalanche detectors*, *Nucl. Instrum. Meth. A* **924** (2019) 380.
- [7] M. Carulla et al., *50 μm thin Low Gain Avalanche Detectors (LGAD) for timing applications*, *Nucl. Instrum. Meth. A* **924** (2019) 373.
- [8] M. Ferrero et al., *Radiation resistant LGAD design*, *Nucl. Instrum. Meth. A* **919** (2019) 16 [[arXiv:1802.01745](#)].
- [9] V.A.K. Temple, *Junction Termination Extension: A New Technique for Increasing Avalanche Breakdown Voltage and Controlling Surface Electric Fields at P-N Junctions*, in proceedings of the *IEEE International Electron Devices Meeting*, Washington, DC, U.S.A., 5–7 December 1977, pp. 423–426.
- [10] M. Lozano et al., *Comparison of radiation hardness of P-in-N, N-in-N and N-in-P silicon pad detectors*, *IEEE Trans. Nucl. Sci.* **52** (2005) 1468.
- [11] P. Fernández-Martínez, D. Flores, S. Hidalgo, V. Greco, A. Merlos, G. Pellegrini et al., *Design and Fabrication of an Optimum Peripheral Region for Low Gain Avalanche Detectors*, *Nucl. Instrum. Meth. A* **821** (2016) 93 [[arXiv:1510.08626](#)].
- [12] G.-F. Dalla Betta, L. Pancheri, M. Boscardin, G. Paternoster, C. Piemonte, N. Cartiglia et al., *Design and TCAD simulation of double-sided pixelated low gain avalanche detectors*, *Nucl. Instrum. Meth. A* **796** (2015) 154.
- [13] R. Dalal, G. Jain, A. Bhardwaj and K. Ranjan, *TCAD simulation of low gain avalanche detectors*, *Nucl. Instrum. Meth. A* **836** (2016) 113.
- [14] T. Wang, X. Wan, H. Jin, H. Li, Y. Sun, R. Liang et al., *Optimization of the cell structure for radiation-hardened power MOSFETs*, *Electronics* **8** (2019) 598.
- [15] B. Jayant Baliga, *Fundamentals of Power Semiconductor Devices*, Springer (2008) [ISBN: 978-0-387-47313-0].